JAAS

ROYAL SOCIETY OF CHEMISTRY

PAPER

View Article Online
View Journal | View Issue

Cite this: *J. Anal. At. Spectrom.*, 2025, **40**, 2716

Mechanism of elemental fractionation during femtosecond laser ablation revealed by high-time-resolution MC-ICP-MS analysis of $^{208}Pb/^{232}Th$ ratios in single particles

Sota Niki *[a] and Takafumi Hirata *[b]

This study investigated the mechanism of elemental fractionation during laser ablation (LA) through elemental analysis of individual particles generated *via* femtosecond laser ablation (fsLA) using a minimised laser spot size of approximately 2 μm. Data acquisition was conducted within a short dwell time of 20 μs using a multiple collector-ICP-mass spectrometer equipped with a high-time-resolution ion counting system (HTR-MC-ICP-MS), which avoids the overlap of signal events from multiple particles. Results obtained from monazite references showed that individual fsLA-generated particles fall into two distinct groups in terms of $^{208}Pb/^{232}Th$: Pb-bearing (volatile-element-rich) *vs.* Pb-depleted (volatile-element-poor). The existence of these two populations is probably the major cause of elemental fractionation in LA. This decoupling is attributed to the different behaviours of volatile and refractory elements during particle generation. Particles that condense from laser-induced vapor plume tend to retain volatile elements (*e.g.*, Pb), whereas particles originating from the molten rim of the ablation pit (material that was molten but not vaporized) are depleted in volatile elements. The data obtained here clearly demonstrated that elemental fractionation is involved in the particle generation process, and hence, using matrix-matched reference materials is essential for obtaining reliable elemental data in LA-ICP-MS.

Received 16th January 2025
Accepted 2nd August 2025

DOI: 10.1039/d5ja00016e

rsc.li/jaas

1 Introduction

Laser ablation is commonly used for sampling of solid materials with a high spatial resolution defined by the laser spot size, and the combined system of LA and mass spectrometry (MS) coupled with an Ar-based ICP ion source, LA-ICP-MS, is utilised as an *in situ* high-sensitivity analytical technique applied to elemental and isotopic measurements.[1]

The main analytical issue associated with LA-ICP-MS is the difference in sensitivity for each element caused by the variation in useful yields, which are defined by the counts of detected ions through LA-ICP-MS per number of atoms originally contained in ablated volumes, depending on physicochemical properties, including melting points, boiling points, and ionisation potentials.[2,3] These parameters are controlling factors of sampling efficiency during LA and the vaporisation and ionisation efficiencies during ICP. The latter deteriorates, especially when particles with sizes larger than the critical size for complete vaporisation and ionisation are introduced into ICP, resulting in the dependency of useful yields on particle size distribution.[4] Thus, the calibration of measured elemental ratios is required for improving the analytical accuracy of multiple-elemental analysis using LA-ICP-MS. Moreover, the useful yields for elements vary depending on sample matrices with different physicochemical properties, and high-quality matrix-matched references are practically necessary for accurate elemental-ratio analysis. This is especially important for U–Th–Pb geochronology, which requires the accurate and precise measurements of Pb/U and Pb/Th for geological samples with analytical uncertainties of a few percent.[5] The useful yields for Pb and U or Th can vary depending on different sampling efficiencies, transport efficiency to ICP (which depend on particle size), and the ionisation efficiency of ICP. Since Pb shows more volatile nature than U and Th, it is easily vaporised compared to U and Th during heating *via* LA, the resulting Pb/U and Pb/Th for ablated materials can be higher than the original composition of the solid sample (*i.e.*, non-stoichiometric sampling), and the measured Pb/U or Pb/Th can increase as the ablation pit becomes deeper.[6] In previous studies, moreover, the coarser LA-generated particles are enriched in refractory elements (*e.g.*, U and Th), and their lower transport efficiency than finer particles results in the further elemental fractionation on Pb/U and Pb/Th during the transport process to ICP.[4,7]

For further investigation on the mechanism of the elemental fractionation involved in fsLA, in this study, the Pb/Th values of

[a]*Division for Chronological Research, Institute for Space-Earth Environmental Research, Nagoya University, Furo-cho, Chikusa-ku, Nagoya 464-8601, Japan. E-mail: niki.sota.t1@f.mail.nagoya-u.ac.jp*

[b]*Geochemical Research Center, The University of Tokyo, 7-3-1 Hongo, Bunkyo-ku, Tokyo 113-0033, Japan*

LA-generated particles were measured. In previous studies, the chemical compositions of LA-generated particles have been determined by the bulk chemical analysis of the LA-generated materials fractionated by particle size,[8] or chemical analysis of the limited number of deposited particles around the LA pits by electron microscopy.[9] As a result, the difference and variation in the chemical compositions of individual LA-generated particles introduced into ICP are still unclear.

For online analysis of LA-generated particles by ICP-MS, a high-time-resolution (HTR) data acquisition system (<100 μs) is required for tracing transient isotope signal profiles within a few hundred microseconds derived from the introduction of nanoparticles into ICP. Moreover, high time resolution is important to minimise the integration of multiple signals emanating from two or more particles. In a pioneering study, online analysis of LA-generated particles by ICP-MS was performed using an HTR single-collector ICP-MS coupled with a femtosecond LA system (wavelength: 1030 nm, 515 nm, and 257 nm).[10] This study determined the size distribution of nanoparticles produced by laser ablation of copper, based on mathematical analysis of the isotope signal profiles. In spite of the importance, there are two main challenges: one is the overlapping of signals derived from multiple particle-introduction events, and the other is the single-element analysis.

To derive accurate elemental ratios for individual LA-generated particles, a new system for high-time-resolution multiple-isotope analysis without the signal overlapping is necessary. Then, in this study, we developed a new protocol for online elemental/isotopic-ratio analysis of individual LA-generated particles based on the combination of an in-house high-spatial-resolution fsLA system and a high-time-resolution multiple-collector ICP-MS system (HTR-MC-ICP-MS). By minimising the laser spot size (*i.e.*, 2 μm), the number of generated particles by a single laser shot is decreased, and the introduction rate of the particles into ICP is reduced. The second point of the multiple collection system is essential for multiple-isotope (multiple-element) analysis to determine the elemental ratios of individual fsLA-generated particles.

In this study, to elucidate the nature of the elemental fractionation related to fsLA, the $^{208}Pb/^{232}Th$ values of individual particles produced *via* fsLA on monazite were analysed by the present technique. Monazite is a lanthanide phosphate mineral with a high Th concentration up to several percentages (wt/wt%) and is commonly used as a ^{232}Th–^{208}Pb geochronometer. In our geochronological community, several well-characterised monazite references with known radioisotope ages, which have the known $^{208}Pb/^{232}Th$ values defined by the radioisotope ages if the contribution of non-radiogenic Pb is negligible, are available. By analysing them, the degree of the elemental fractionation involved in the particle-generation process through fsLA was evaluated.

2 Experimental

2.1 Overview of the fsLA-HTR-MC-ICP-MS system

For multiple-isotope analyses of individual fsLA-generated particles, in this study, an in-house high-spatial-resolution fsLA system was combined with an HTR-MC-ICP-MS system (Fig. 1). The in-house high-spatial-resolution fsLA system is composed of an Yb:KGW femtosecond laser system (pulse width: 250 fs) with a laser wavelength (λ) of 260 nm and a beam diameter (D) of 4.2 mm before focusing, galvanometric optics, and a short-focal-length objective lens. The focal length of the objective lens (f) is 10 mm, which is ten times shorter than that of a conventional one. The theoretical focused beam size (d) is *ca.* 1 μm according to the equation of $d = 4\lambda f/(\pi D)$. From the photograph of the laser ablation pits (Fig. 2), the actual single-shot laser spot size on monazite is *ca.* 2 μm in diameter.

The HTR-MC-ICP-MS system used in this study is a modified Nu Plasma II ICP-MS manufactured by Nu Instruments (Wrexham, U.K.).[11–13] The HTR-MC-ICP-MS system has three HTR Daly ion counters and three HTR secondary-electron-multiplier (SEM) detectors. This detector configuration (summarised in Fig. 1(c)) allows simultaneous collection of ^{232}Th, ^{208}Pb, ^{206}Pb, and $^{204}Pb + {}^{204}Hg$ signals. The Daly ion counters have a wider dynamic range and a longer-term gain stability compared to the

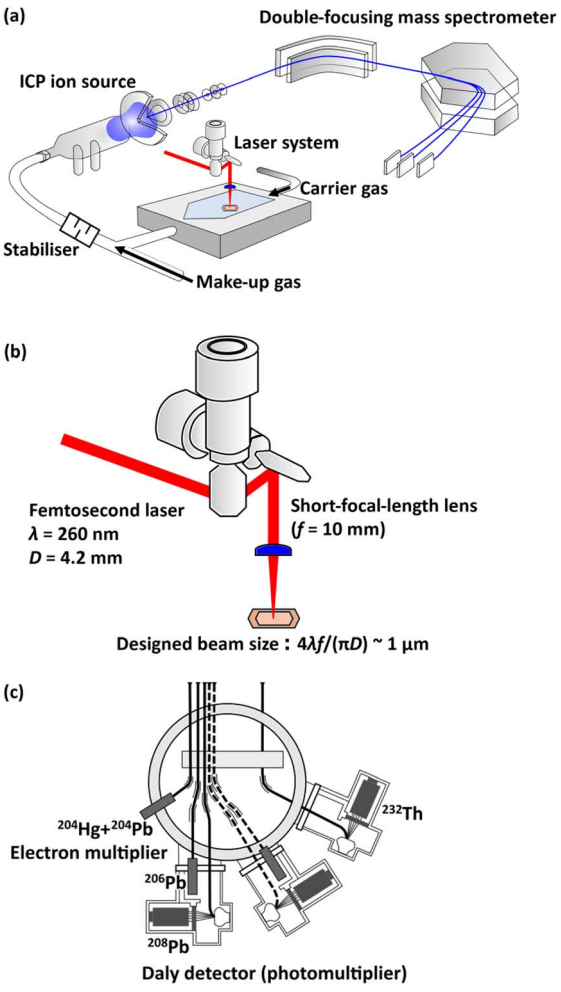

Fig. 1 Schematic of the fsLA-HTR-MC-ICP-MS system. (a) Overview of the fsLA-HTR-MC-ICP-MS system. (b) Schematic of the high-spatial-resolution fsLA system. (c) Cup configuration of the HTR-MC-ICP-MS system for simultaneous detection of Th–Pb isotopes.

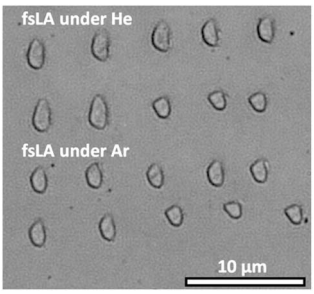

Fig. 2 Photographic image of the ablation pits for the 16-F-6 monazite with a diameter of about 2 μm. The ten spots in the upper and lower halves correspond to the pits made by fsLA under He and Ar atmospheric gases, respectively.

SEM ion counters, and hence, two Daly detectors, D5 and D2, are utilised for monitoring two important isotopes of ^{232}Th and ^{208}Pb, respectively. In addition to this, two SEM detectors, IC3 and IC4, are used for measuring ^{206}Pb and ^{204}Pb + ^{204}Hg, respectively. The cup configuration is summarised in Fig. 1(c).

2.2 Operational settings of the fsLA-HTR-MC-ICP-MS system

The operational conditions for the fsLA-HTR-MC-ICP-MS system are summarised in Table 1. For the in-house high-spatial-resolution fsLA system, the fluence is *ca.* 4 J cm^{-2}, and the number of laser shot is one (single-shot fsLA) for each spot. The carrier gas used for atmospheric gas in the sample chamber was He or Ar with a flow rate of 1 L min^{-1}. The make-up gas with a flow rate of 1 L min^{-1} was added to the atmospheric gas outside the sample chamber. Argon was used as a make-up gas in the case of He carrier gas or *vice versa*, for keeping the plasma gas condition through all experiments. Between the sample chamber and ICP, a particle slowing-down device (*i.e.*, signal stabiliser)[14] was inserted to broaden the particle transit time, and thus, further reduce overlapping of particle-introduction events.

For the HTR-MC-ICP-MS system, the dwell time on each detector was set to 20 μs. After each single-shot ablation, signals were recorded for 30 seconds to capture all particle events. The non-extended-type refresh-time correction was applied to all ion counters,[11,12,15] using refresh times of 20.0 ns (D5), 10.8 ns (D2), 14.7 ns (IC3), and 15.4 ns (IC4).

2.3 Monazite references

The monazites analysed in this study were 16-F-6 monazite reference,[16] Namaqualand monazite reference,[17] and 44069 monazite reference.[18] The 16-F-6 monazite is a well-characterised reference used for geochronological studies, and has the precise U–Pb age of 2842.9 ± 0.3 Ma determined by isotope-dilution thermal ionisation mass spectrometry (ID-TIMS), and the reported Th concentration is *ca.* 24 000 μg g^{-1}.[16] The Namaqualand monazite has the highest Th concentration among three monazite references, and the U–Pb age of *ca.* 1033 Ma was determined by secondary ionisation mass spectrometry.[17] The Namaqualand monazite is commonly used for a secondary reference of the chemical Th–U-total Pb isochron method using electron probe microanalysis, and one reported age in a previous study is 1020 ± 41 Ma.[19] The 44069 monazite has a Th concentration ranging from 10 000 to 50 000 μg g^{-1}, and the ID-TIMS U–Pb age is 424.9 ± 0.4 Ma.[18] The calculated ^{208}Pb/^{232}Th values for the 16-F-6, Namaqualand, and 44069 monazites are 0.15102, 0.05244, and 0.02124, respectively, based on the radioisotope ages and the decay constant of ^{232}Th

Table 1 Operational setting for LA-ICP-MS

(a) ICP-MS	
HTR-MC-ICP-MS instrument	Nu Plasma II (Nu Instruments, U.K.)
Sample introduction	Laser ablation
RF power	1300 W
Coolant gas flow	15.0 L min^{-1}
Auxiliary gas	0.8 L min^{-1}
Detection system	Multiple ion counting array
Monitored mass-to-charge ratio	204, 206, 208, and 232 Da
Detectors	Two Daly detectors (D), and two full size multipliers (IC) D2 for ^{208}Pb, IC3 for ^{206}Pb IC4 for ^{204} (Hg + Pb), and D5 for ^{232}Th
Dwell time	20 μs
(b) Laser ablation	
Laser ablation system	An in-house laser system (FAB Instrument, Tokyo, Japan)
Laser medium	Yb:KGW
Laser wavelength	260 nm (4th harmonic generation)
Pulse width	250 fs
Fluence	*ca.* 4 J cm^{-2}
Repetition rate	1000 Hz
Carrier gas	1.0 L min^{-1} (He or Ar)
Make-up gas flow	1.0 L min^{-1} (Ar or He)
Spot diameter	*ca.* 2 μm

(4.9475×10^{-11} per year)[20] under the assumption of the concordance in the U–Pb and Th–Pb isotope systematics for the monazite references. Ten-times repeated analyses with a spot size of *ca.* 2 μm were performed on three monazite references (Fig. 2).

2.4 Data reduction

Elemental/isotopic-ratio analyses were performed on signal events that emanated from single small particles produced through fsLA. The data reduction begins with finding peaks with a higher signal intensity than that of the signal intensities at the preceding and following time slices through the time-resolved isotope profiles. In this study, this primary peak detection was conducted for the summed signal intensities of ^{208}Pb and ^{232}Th, and when the combined signal intensities of ^{208}Pb and ^{232}Th exceeded a certain threshold, the signal peaks were treated as signals derived from particle-introduction events. Thresholds were set by examining 30 second gas-blank signal profiles and choosing a cutoff that yields <1 false event in the blank period. Based on this, the ^{208}Pb + ^{232}Th count threshold was set to 6 counts for He atmospheric gas and 8 counts for Ar atmospheric gas. Subsequently, we filtered out any small 'sub-peaks' that occurred within the duration of a much larger peak. Such sub-peaks can otherwise cause erroneous event counts or skewed Pb/Th values. Specifically, if a minor signal occurred within the width of a major peak (defined as the full width at 0.5% of the peak's maximum intensity), it was not counted as a separate event. Finally, the signal counts of ^{232}Th, ^{208}Pb, ^{206}Pb, and ^{204}Pb + ^{204}Hg for remaining particle-derived signals were calculated by the summation of the signal counts and the subtraction of the gas-blank signal intensity within the range of the time slices, just including the signal width of the peak.

We estimated the size (volume and equivalent diameter) of individual particles (for the 16-F-6 monazite) using the measured ^{232}Th counts and the known composition of the monazite. This calculation assumes that there is negligible fractionation among the major matrix components of monazite during fsLA, so each particle's composition (apart from volatile Pb loss) is essentially that of bulk monazite. Eqn (1) and (2) were used as follows:

$$V = \frac{I_{\mathrm{Th}}}{f} \times \frac{m_{\mathrm{Th}}}{N_{\mathrm{A}} C_{\mathrm{Th}} \rho} \quad (1)$$

$$d = \sqrt[3]{\frac{3V}{4\pi}} \times 2 \quad (2)$$

where V is the reduced volume of a single particle, I_{Th} is the signal count of ^{232}Th for a single particle, f is the ion transmission through the ICP-MS system, m_{Th} is the molar mass of Th (232.0385 g mol^{-1}), N_{A} is the Avogadro constant (6.02×10^{23} mol^{-1}), C_{Th} is the thorium concentration (16-F-6 monazite; 24 000 μg g^{-1}), ρ is the density of monazite (*ca.* 5 g cm^{-3}), and d is the reduced diameter.

The ion transmission through the ICP-MS system was approximated by applying the useful yield of the fsLA-HTR-MC-ICP-MS system determined from the analysis of NIST SRM 610 by the present technique under the conditions of He atmospheric gas and Ar make-up gas. The actual value of the useful yield for ^{232}Th was 0.065% calculated by dividing the signal counts of ^{232}Th by the estimated number of ^{232}Th atoms contained in the ablated volumes of NIST SRM 610. One notable thing is that this value includes the loss of LA-generated particles during the transportation and should be a lower limit of the ion transmission through the ICP-MS system, resulting in the overestimation of the particle size. The transport efficiency of the fsLA-generated particles should be several tens of percent or more, and the reduced particle size may deviate from the actual size by a factor of up to two.

3 Results and discussion

3.1 Fractionation on Pb/Th *via* an fsLA particle-generation process

Fig. 3(a) illustrates the signal intensity profiles for ^{232}Th, ^{208}Pb, ^{206}Pb, and ^{204}Pb obtained through single-shot fsLA on the 16-F-6 monazite reference under the He atmosphere, suggesting the presence of numerous transient peaks emanating from the particle-introduction events. Fig. 3(b) is the enlarged-scale version of the time-resolved signal profile, demonstrating that the acquisition of signal intensity data for individual particles could be made. The contribution of signal overlap is not greater than 2% based on the assumption that (I) the time duration of signal events is 100 μs, and (II) the number of signal events per single second is 200.

The resulting time-resolved multiple-isotope signal profile suggests the presence of at least two types of particles; (I) Pb-bearing particles with both the ^{232}Th and ^{208}Pb signals and (II) Pb-depleted particles with ^{232}Th signals and without ^{208}Pb signals demonstrated in Fig. 3(c). In Fig. 4, the signal counts of ^{232}Th for each particle event detected through ten-times repeated analyses of the 16-F-6 monazite reference are plotted

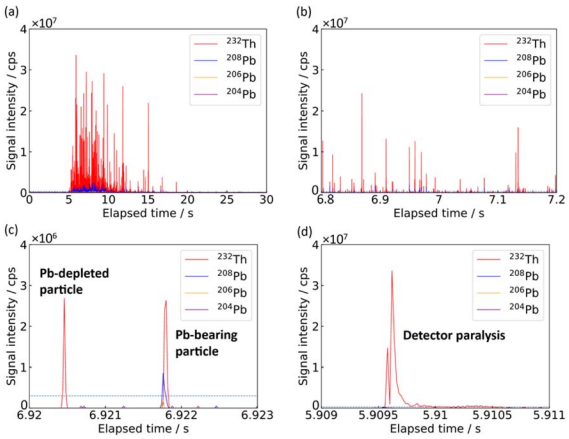

Fig. 3 Multiple-signal intensity profiles of single-shot LA on the 16-F-6 monazite acquired through HTR-MC-ICP-MS. (a) Whole time-resolved isotope signal profile after single-shot LA. (b) Enlarged version of the signal intensity profiles for the signal events. (c) Examples for signal profiles derived from a Pb-depleted particle and a Pb-bearing particle. (d) Saturated signal profile due to detector paralysis.

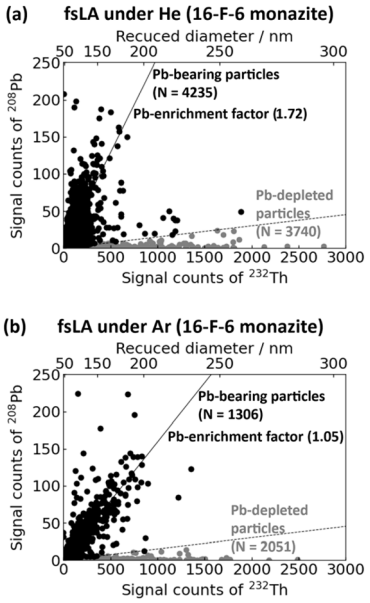

Fig. 4 Signal counts of ^{232}Th and ^{208}Pb for each fsLA-generated particle under (a) He and (b) Ar atmospheres in the ten-spot analyses of the 16-F-6 monazite reference. Black and grey circles demonstrate Pb-bearing particles and Pb-depleted particles, respectively. The dashed line shows the threshold line set at ^{208}Pb/^{232}Th being 0.015102 as the one-tenth of the reference ^{208}Pb/^{232}Th value. The slope of the black lines indicates the Pb-enrichment factor for Pb-bearing particles.

against those of ^{208}Pb. Fig. 4(a) and (b) correspond to the results obtained *via* fsLA under the He and Ar atmospheres, respectively. The data points plotted in Fig. 4(a) and (b) clearly show the decoupling of the Pb/Th values for the fsLA-generated particles. The two decoupled components can be explained by the different behaviour of Th and Pb through fsLA reflecting the different physicochemical behaviour of Th and Pb through fsLA. In terms of the volatility, Th is a highly refractory element, while Pb is a volatile element. The melting point of ThO_2 is *ca.* 3700 K,[21] and the melting and boiling points of PbO are *ca.* 1200 K and *ca.* 1800 K, respectively.[22] As for the monazite, as well as ThO_2, the major components of monazite (rare-earth-element phosphate) have a higher melting point (2200–2400 K)[23] than the boiling point of PbO. Owing to the difference in the volatility, Pb and Th behave differently during the melting, vaporisation and subsequent condensation through fsLA.

Two possible particle-generation mechanisms could account for the observed Pb/Th decoupling. (1) Fractional condensation from the vapor phase: after material is vaporized by fsLA, the refractory components condense first, followed by the volatile components. Early condensed particles would thus be depleted in volatiles like Pb, while later-condensed particles become enriched in Pb. This scenario, however, would require that the early-formed refractory-rich particles are somehow removed or separated from the plume before the volatile-rich particles condense, otherwise both types might equilibrate. (2) Dual-phase particle generation: Pb-bearing particles originate from vaporized material at the ablation site, while Pb-depleted particles derive from the residual molten material. As the fs laser has a Gaussian beam profile, the central irradiated zone experiences higher fluence (and temperature) than the periphery. The centre of the ablation spot reaches a temperature of several thousands of kelvins, causing complete evaporation (or sublimation) of that material. Meanwhile, the rim of the ablation spot is exposed to a lower energy density; it becomes molten but not fully vaporized (surrounding material affected by heat may also melt).[24,25] The molten portion of monazite can thus produce droplets that are depleted in Pb. When the liquid phase of monazite is produced, Pb can be preferentially evaporated from the molten layer because the boiling point of PbO is lower than the melting points of both the monazite and ThO_2. This is followed by the production of Pb-depleted particles from the molten layer, and the particles condensed from the fsLA-induced vapor phase should be enriched in Pb.

The following evidence from our experiments supports this second mechanism: the size distribution of the detected particles also provides several key information concerning the particle generation process *via* fsLA. In Fig. 5, the reduced size distribution of the detected Pb-depleted particle (a) and Pb-bearing particle (b) are given. Hence, the reduced diameters of the individual particles are plotted on the *x*-axis, and the number of detected particles through ten-spot analyses on the 16-F-6 monazite is plotted on the *y*-axis. In this study, the threshold for Pb-depleted and Pb-bearing particles is set as being less or greater than one-tenth of the original ^{208}Pb/^{232}Th value calculated from the reported radioisotope age of the

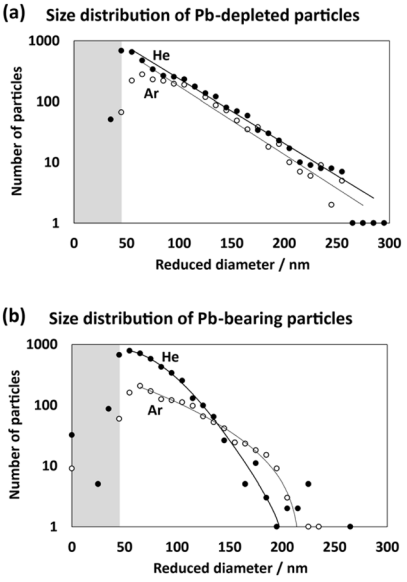

Fig. 5 Size distribution of (a) Pb-depleted particles and (b) Pb-bearing particles. The reduced diameter for detected particles calculated from the signal counts of ^{232}Th is plotted on the *x*-axis, and the number of particles in the ten-spot analyses of the 16-F-6 monazite is plotted on the *y*-axis. The closed and open circles refer to the data obtained by fsLA under He and Ar atmospheres, respectively. The data plotted on the grey-coloured areas correspond to particle signals whose intensity is close to the baseline, and the number of particles in those ranges can be underestimated compared to the actual number.

monazite reference. For the Pb-depleted particles, the size distributions for both the He and Ar atmospheres are similar to each other, as shown in Fig. 5(a). The similarity regardless of the atmospheric gases indicates that the Pb-depleted particles were formed without the involvement of the gas phase. This strongly supports the second possibility of the Pb-depleted particles formed *via* the molten rim portion.

The presence of the particles being enriched in the volatile element suggests that the LA-induced gas phase should be enriched in volatile elements, and thus, the Pb-bearing particles should be partly derived from the LA-induced gas phase. For the Pb-bearing particles demonstrated in Fig. 5(b), the number of larger particles than 150 nm generated under Ar atmospheric gas is greater than that of the particles generated under He atmospheric gas. This clear difference in the size distributions can be explained by particle generation *via* the condensation process. Argon has higher viscosity and lower thermal conductivity than He, and hence, the volume of the LA-induced plume under Ar is smaller than He due to the slow diffusion and heat accumulation. This implies that, in the LA-induced plume, the number of atoms per unit volume under the Ar atmosphere is greater than that under the He atmosphere, and the resulting particles generated through condensation after cooling of the LA-induced plume can become larger.

Fig. 6 illustrates the proposed mechanism in this study for the elemental fractionation through the particle-generation process during fsLA. After femtosecond laser irradiation on the sample surface, the central area of the LA pit vaporises, and the rim portion remains molten. The volatile elements including Pb with the lower boiling points than the melting point of the sample matrix also vaporise from the molten portion. Then, from the LA-induced vapor phase, volatile-element-bearing particles are generated *via* condensation, while the volatile-element-depleted particles are released from the molten rim area.

Previous studies on electron-microscopic analyses of LA-generated particles favour the proposed mechanism of the elemental fractionation in this study. In previous research, the elemental fractionation of Zn and Cu through LA has been well investigated by electron-microscopic observations on LA-generated particles. Zn has a lower boiling point (*ca.*1200 K) than the melting point of Cu (*ca.* 1400 K), and these physico-chemical properties are similar to those of Pb and Th. In terms of the chemical compositions of LA-generated particles, finer particles tend to be depleted in Zn (volatile-element-depleted) and *vice versa* in the cases of both the nanosecond LA and femtosecond LA.[8,26] This dependency on particle size is explained by our data of the reduced particle size distributions of the Pb-depleted and Pb-bearing particles. Another important electron-microscopic study showed two types of particles generated *via* fsLA on brass: (I) agglomeration of fine particles and (II) spherical coarse particles with a diameter of a few hundred nanometres.[27] The presence of the spherical coarse particles strongly indicates the melting process through the particle generation during fsLA. This observational study also favours the ejection of the molten particles depleted in volatile elements suggested by our data.

If the transport efficiencies of the volatile-element-bearing and volatile-element depleted particles are different, the bulk chemical composition of the laser induced particles can deviate from the original composition of the ablated material. Considering from Fig. 5(a) and (b), the reduced size of the volatile-element-depleted particles tends to be larger than that of the volatile-element-bearing particles, and this can result in the lower transport efficiency of the volatile-element-depleted particles. Moreover, depending on the melting and boiling points of sample matrices, the mass ratios of the LA-induced vapor phase to the molten phase vary, and the difference among sample matrices (*e.g.*, monazite, zircon, or glass) can require the determination of the calibration factors for elemental ratios based on reference materials for each matrix to acquire accurate analytical results even when utilising ultraviolet fsLA[28] with reduced thermal loading on the sample surface during LA, resulting in the high sampling efficiency with less dependence on the physicochemical properties of sample matrices and elements of interest.[29] Compared to fsLA, nanosecond LA causes more severe thermal loading, and the contribution of the LA-induced molten phase should be larger. Further investigation on the elemental fractionation using different types of LA will be necessary.

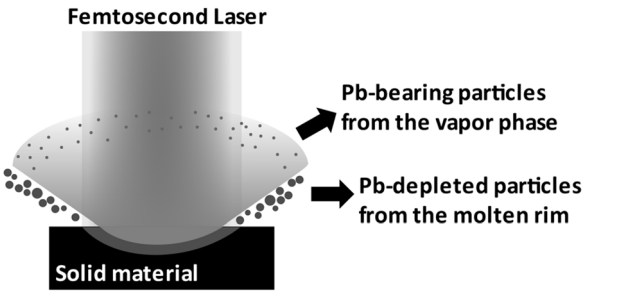

Fig. 6 Schematic of the ablation process using femtosecond laser with a Gaussian beam profile.

3.2 ^{232}Th–^{208}Pb age determination of monazite

For each ablation spot (single laser shot), we summed the ^{232}Th and ^{208}Pb counts from all particle events to obtain a total ^{208}Pb/^{232}Th. We calibrated this ratio using our measurements of the 16-F-6 monazite, which has a known age and thus known ^{208}Pb/^{232}Th, and converted the ratio to an equivalent ^{232}Th–^{208}Pb age for the sample. The resulting weighted-average ^{232}Th–^{208}Pb ages of ten-spot repeated analyses are 1161 ± 120 Ma and 265 ± 23 Ma (95% conf., $N = 10$) with the mean squared weighted deviation (MSWD) values of 7.2 and 2.4 for the Namaqualand monazite and the 44069 monazite, respectively. These obtained ages of the Namaqualand monazite and the 44069 monazite are significantly older and younger than the reference values, respectively. The systematic deviation of ^{208}Pb/^{232}Th is partly attributed to the counting loss of high-intensity signals of ^{232}Th (>10^7 cps) emanating from coarse particles introduced into ICP-MS. Fig. 3(d) shows the signal profile of ^{232}Th exceeding 10^7 cps, and this bimodal profile is

due to the counting loss of ions, originating from the detector paralysis. The contribution of the counting loss becomes more significant as the Th concentration increases, resulting in systematically higher $^{208}Pb/^{232}Th$ values (*i.e.*, older age values) in higher-Th-concentration samples and younger age values in lower-Th-concentration samples. This trend for systematic deviation in $^{232}Th–^{208}Pb$ ages is consistent with the obtained data for the Namaqualand monazite (high-Th monazite) and the 44069 monazite (low-Th monazite).

For accurate isotopic-ratio measurements, careful correction of counting loss due to detector refresh time is desired. In this study, the counting loss was primarily corrected based on the non-extended-type detector refresh time for each pulse-counting detector. The counting loss derived from the non-extended-type refresh time of pulse-counting ion counters is corrected for each isotope signal intensity at each time slice. This is necessary for the accurate determination of Pb/U or Pb/Th for U- and Th-enriched minerals (*e.g.*, zircon and monazite), since the abundances of Pb, and U or Th differ by several orders of magnitude.[11,12] Then, for monitoring LA signals, Hirata *et al.* (2021) demonstrated the importance of high-time resolution analysis to accurately correct the counting loss for transient high-intensity signals (>10^6 cps) through the U–Pb age determination of zircon references (U concentration: 80–1000 μg g^{-1}) even if the averaged signal intensity is low enough (<10^6 cps) with a negligible counting loss in the conventional way.[15] Despite the success of the counting-loss correction using the HTR analysis in the previous study, for monitoring the high-intensity signals of ^{232}Th with more than 10^7 cps derived from the major component of the fsLA-generated monazite particles in this study, systematic deviation due to the counting loss derived from the detector paralysis is significant. This is attributed to the extended-type detector refresh time, and further correction should be required. However, identifying the nonlinear formula for the correction of the counting loss and determining the actual extendable refresh time are practically difficult, and this study does not propose a correction formula for the counting loss.

The contribution of the counting loss is particularly serious for the coarse particles, and by excluding the isotope data for Pb-depleted particles, the systematic error due to the counting loss can be reduced. Then, the isotope data of the Pb-bearing particles without the Pb-depleted particles were used for the determination of $^{208}Pb/^{232}Th$. First, the signal counts of ^{208}Pb and ^{232}Th for the Pb-bearing particles are summed. Then, the correction factor of $^{208}Pb/^{232}Th$ was calculated from the ratio of the reference $^{208}Pb/^{232}Th$ value and the signal-count $^{208}Pb/^{232}Th$ ratio of the Pb-bearing particles for the 16-F-6 monazite reference. This correction factor means the Pb enrichment factor for the Pb-bearing particles, and the Pb enrichment factor is identical to unknown monazite samples if the matrix of the reference and unknown samples are similar (*i.e.*, matrix-matched calibration) in terms of the chemical compositions and physicochemical properties. The actual correction factor for $^{208}Pb/^{232}Th$ calculated from the ten-spot analyses of the 16-F-6 monazite reference is 1.72 ± 0.12 (1 SD), as shown in Fig. 4(a). This value is consistent with the Pb-enrichment factors

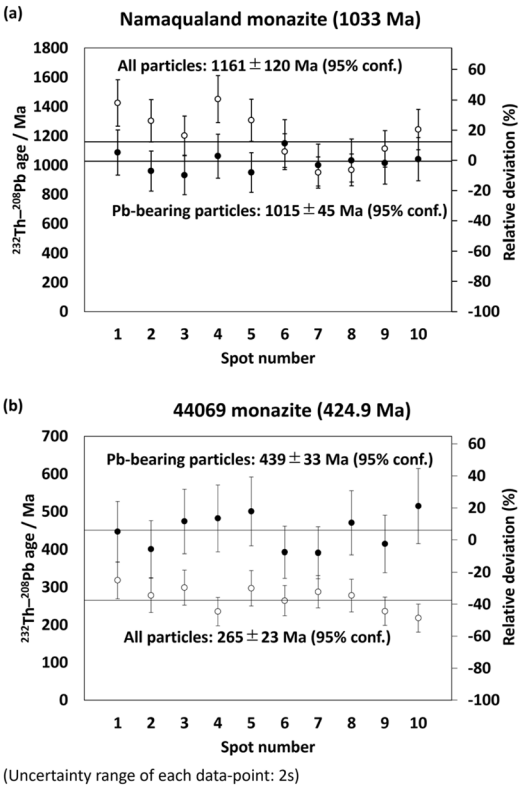

Fig. 7 Obtained $^{232}Th–^{208}Pb$ ages from the ten-spot analyses of (a) Namaqualand monazite and (b) 44069 monazite. The open circles indicate the age values calculated from all detected particles. The closed circles demonstrate those calculated from the Pb-bearing particles. The uncertainty range for each data point is 2 s. The black horizontal lines indicate the weighted average value of the $^{232}Th–^{208}Pb$ ages. The relative deviation from the previously reported ages is shown in the right-side *y*-axis.

for the Namaqualand monazite and the 44069 monazite, as shown in Fig. 8. Finally, the obtained weighted-average $^{232}Th–^{208}Pb$ ages were 1015 ± 45 Ma and 439 ± 33 Ma (95% conf., $N = 10$) with the MSWD values of 0.81 and 1.3 for the Namaqualand monazite and the 44069 monazite (Fig. 7), and these age values are in good agreement with the previously reported age values of 1033 Ma and 424.9 Ma, respectively. In this isotope-ratio calculation scheme, the cutoff threshold of the Pb-bearing and Pb-depleted particles is set at one-tenth of the reference $^{208}Pb/^{232}Th$ values for monazites. As shown in Fig. 9, when the cutoff threshold is changed, the resulting isotope ratios remain in agreement with the reference values within ±10% in the range of the cutoff threshold from 0.05 to 0.5. The resulting isotope ratios are not likely to be dependent on the cutoff threshold because of the strong bimodality of $^{208}Pb/^{232}Th$.

In summary, the isotope signal profiles of LA-ICP-MS are not derived from stable ion currents, but are composed of transient signals originating from numerous LA-generated particles. Thus, for accurate isotope-ratio analysis or elemental-ratio analysis, the correction of counting-loss for transient high-intensity signals was resolved by HTR-ICP-MS even when the

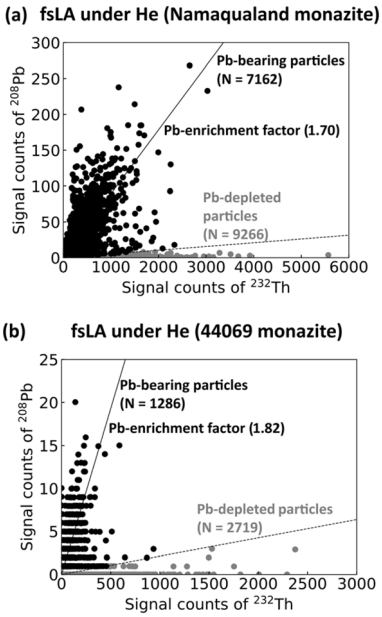

Fig. 8 Signal counts of ^{232}Th and ^{208}Pb for each fsLA-generated particle under an He atmosphere in the ten-spot analyses of (a) the Namaqualand monazite and (b) the 44069 monazite. Black and grey circles indicate Pb-bearing particles and Pb-depleted particles, respectively. The dashed line shows the threshold line set at ^{208}Pb/^{232}Th being (a) 0.005244 and (b) 0.002124 as the one-tenth of the reference ^{208}Pb/^{232}Th values. The slope of the black lines means the Pb-enrichment factors for Pb-bearing particles.

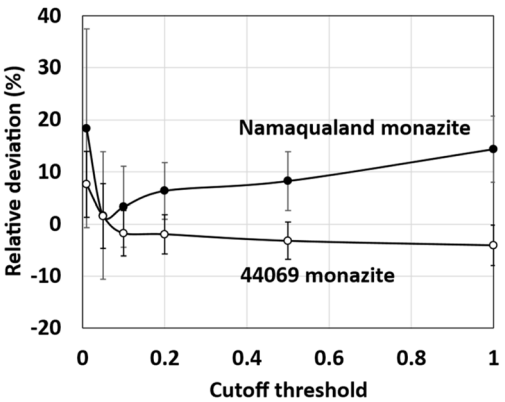

Fig. 9 Relative deviation of the resulting ^{232}Th–^{208}Pb ages from the reference values for two reference monazites depending on the cutoff threshold of the Pb-bearing and Pb-depleted particles. The *x*-axis represents the cutoff threshold expressed as a proportion of the reference values. Closed circles and open circles represent the data of Namaqualand monazite and 44069 monazite, respectively. The uncertainty range corresponds to a 95% confidence level.

averaged signal intensity is lower than 10^6 cps with apparently negligible contribution of the counting loss. Especially for the measurement of major components (*i.e.*, >10 000 μg g^{-1}), the introduction of coarse particles must produce higher signal intensities than 10^7 cps, resulting in a significant systematic error due to the extended-type detector refresh time. In this study, by distinguishing the Pb-bearing particles from the time-resolved signal profiles based on the HTR-MC-ICP-MS system and summing the ^{208}Pb and ^{232}Th signal counts of the Pb-bearing particles, the accurate matrix-matched correction of ^{208}Pb/^{232}Th for monazite samples was achieved. In addition to the Th–Pb dating of monazite, the analytical protocol using LA-HTR-MC-ICP-MS must be important for the accurate elemental-ratio measurements, such as Pb/U and Zn/Cu, which require the analysis of both the volatile and refractory elements. Further systematic studies on the elemental fractionation using this protocol will be necessary for various matrices and combinations of elements.

4 Conclusion

In this study, the mechanism of elemental fractionation between Pb and Th was investigated through online multiple-isotope analysis using a high-spatial-resolution fsLA system and an HTR-MC-ICP-MS system with a dwell time of 20 μs. This system allowed us to analyze individual particles produced by a single fs laser shot on monazite (spot size 2 μm). The main conclusions are summarized as three key points:

(1) The particles generated *via* fsLA on monazite are classified into two groups: Pb-bearing and Pb-depleted particles. The decoupling of Pb/Th is due to the different behaviour of the elements during the fsLA process. The Pb-bearing (volatile-element-bearing) particles are generated from the fsLA-induced vapor phase, and the Pb-depleted (volatile-element-depleted) particles come from the molten rim portion of the ablation pit.

(2) Even if the averaged signal intensity for the whole isotope signal profile does not exceed 10^7 cps, the counting loss for the transient high-intensity isotope signals of coarse particles is significant. This is the source of systematic error for isotope analysis. Especially for the ^{232}Th–^{208}Pb age determination of monazite, the counting loss of ^{232}Th for coarse Pb-depleted particles is the main source of the analytical error in ^{208}Pb/^{232}Th depending on the Th concentration of monazite samples.

(3) With the calibration of ^{208}Pb/^{232}Th based on the signal summation of the Pb-bearing particles, the accurate ^{232}Th–^{208}Pb age determination with a spot size of *ca.* 2 μm can be made for the Namaqualand monazite (1033 Ma) and the 44069 monazite (424.9 Ma). For the accurate age determination, characterising each particle signal event based on the HTR-MC-ICP-MS system is essential.

Conflicts of interest

There are no conflicts to declare.

Data availability

The data supporting this article have been included as part of the SI.

Supplementary information is available and includes the time-resolved isotope signals shown in Fig. 3, as well as the

signal count data of all particle signal events used in Fig. 4, 5 and 7–9. See DOI: https://doi.org/10.1039/d5ja00016e.

Acknowledgements

We are grateful to Dr Tsuyoshi Iizuka, Dr Tetsuo Kawakami, Mr Shumpei Kudo, and Dr Takeshi Imayama for providing the monazite references used in this study. This work was financially supported, in part, by a Grant-in-Aid for Scientific Research (JP21H04511) from the Ministry of Education, Culture, Sports, Science and Technology, Japan.

References

1 A. L. Gray, *Analyst*, 1985, **110**, 551–556.
2 P. Arrowsmith, *Anal. Chem.*, 1987, **59**, 1437–1444.
3 S. M. Eggins, L. P. J. Kinsley and J. M. G. Shelley, *Appl. Surf. Sci.*, 1998, **127–129**, 278–286.
4 M. Guillong and D. Günther, *J. Anal. At. Spectrom.*, 2002, **17**, 831–837.
5 S. E. Jackson, N. J. Pearson, W. L. Griffin and E. A. Belousova, *Chem. Geol.*, 2004, **211**, 47–69.
6 T. Hirata and R. W. Nesbitt, *Geochim. Cosmochim. Acta*, 1995, **59**, 2491–2500.
7 H.-R. Kuhn and D. Günther, *J. Anal. At. Spectrom.*, 2004, **19**, 1158–1164.
8 J. Koch, A. von Bohlen, R. Hergenröder and K. Niemax, *J. Anal. At. Spectrom.*, 2004, **19**, 267–272.
9 J. Košler, M. Wiedenbeck, R. Wirth, J. Hovorka, P. Sylvester and J. Míková, *J. Anal. At. Spectrom.*, 2005, **20**, 402–409.
10 A. Donard, F. Claverie, F. Pointurier, C. B. Frayret, B. Svatosova and C. Pécheyran, *Anal. Chem.*, 2017, **89**, 8791–8799.
11 H. Obayashi, M. Tanaka, K. Hattori, S. Sakata and T. Hirata, *J. Anal. At. Spectrom.*, 2017, **32**, 686–691.
12 K. Hattori, S. Sakata, M. Tanaka, Y. Orihashi and T. Hirata, *J. Anal. At. Spectrom.*, 2017, **32**, 88–95.
13 T. Hirata, S. Yamashita, M. Ishida and T. Suzuki, *Mass Spectrom.*, 2020, **9**, A0085.
14 A. Tunheng and T. Hirata, *J. Anal. At. Spectrom.*, 2004, **19**, 932–934.
15 T. Hirata, S. Niki, S. Yamashita, H. Asanuma and H. Iwano, *J. Anal. At. Spectrom.*, 2021, **36**, 70–74.
16 A. Simonetti, L. M. Heaman, T. Chacko and N. R. Banerjee, *Int. J. Mass Spectrom.*, 2006, **253**, 87–97.
17 M. Knoper, R. A. Armstrong, M. A. G. Andreoli and L. D. Ashwal, *J. Afr. Earth Sci.*, 2000, **31**, 38–39.
18 J. N. Aleinikoff, W. S. Schenck, M. O. Plank, L. Srogi, C. M. Fanning, S. L. Kamo and H. Bosbyshell, *Geol. Soc. Am. Bull.*, 2006, **118**, 39–64.
19 T. Hokada, K. Horie, T. Adachi, Y. Osanai, N. Nakano, S. Baba and T. Toyoshima, *Precambrian Res.*, 2013, **234**, 183–209.
20 R. H. Steiger and E. Jäger, *Earth Planet. Sci. Lett.*, 1977, **36**, 359–362.
21 T. R. Pavlov, T. Wangle, M. R. Wenman, V. Tyrpekl, L. Vlahovic, D. Robba, P. Van Uffelen, R. J. M. Konings and R. W. Grimes, *Sci. Rep.*, 2018, **8**, 5038.
22 D. Risold, J.-I. Nagata and R. O. Suzuki, *J. Phase Equil.*, 1998, **19**, 213–233.
23 Y. Hikichi and T. Nomura, *J. Am. Ceram. Soc.*, 1987, **70**, C252–C253.
24 A. Ben-Yakar, A. Harkin, J. Ashmore, R. L. Byer and H. A. Stone, *J. Phys. D: Appl. Phys.*, 2007, **40**, 1447.
25 M. Park, M. M. Balkey, X. Mao, C. P. Grigoropoulos and V. Zorba, *Appl. Phys. Lett.*, 2021, **119**, 224103.
26 C. Liu, X. Mao, S. S. Mao, R. Greif and R. E. Russo, *Anal. Chem.*, 2005, **77**, 6687–6691.
27 M. E. Shaheen and B. J. Fryer, *Laser Part. Beams*, 2012, **30**, 473–479.
28 J. Koch, M. Wälle, J. Pisonero and D. Günther, *J. Anal. At. Spectrom.*, 2006, **21**, 932–940.
29 R. E. Russo, X. Mao, J. J. Gonzalez and S. S. Mao, *J. Anal. At. Spectrom.*, 2002, **17**, 1072–1075.